Sensitivity and Lift-off Robustness of Magnetic Resonance Circuit Topologies for Enhanced WPT-Based ECT Systems

Lawal Umar Daura, *Member IEEE*, Yichuang Sun, Senior *Member IEEE,*
Gui Yun Tian, Senior Member, Emmanuel T Ibrahim, Monika Roopak, Changrong Yang

***Abstract*—**Electromagnetic sensors' response is affected by lift-off variations, which are caused by nonmagnetic coating thickness, surface roughness or sensor vibrations. These variations affect eddy current testing (ECT) sensitivity, defect quantification and reconstruction of material properties. This paper compares different magnetic resonance circuit (MRC) topologies as signal conditioning for improving ECT system response to various lift-offs. The MRC is designed to operate at maximum energy, with the potential of several resonances, which lead to enhanced response for optimal and multiple feature extraction, improving signal-to-noise ratio (SNR) and increasing sensitivity to cracks. The proposed paper designs and investigates the effect of different MRC topologies connected to ECT systems to inspect a steel block with surface cracks. The performance comparison of the proposed systems provides the advantages and limitations of different MRC approaches for multiple resonance potentials, higher SNR and response sensitivity at different lift-off distances. The advanced MRC, featuring series and shunt topologies in each transmit and receive coil, is the most immune to noise, with an SNR of 49.9 dB at a 3.4 mm lift-off using its first peak frequency feature. Its response is less crack-sensitive, with a sensitivity of up to 1.5% at 0.6 mm lift-off.

***Index Terms*—**Eddy current testing (ECT), feature extraction, multiple resonances, non-destructive testing, signal-to-noise (SNR), wireless power transfer (WPT) topology.

I. Introduction

Eddy Current Testing (ECT) is a well-established non-destructive testing (NDT) technique widely employed for the inspection and evaluation of conductive materials for safety and maintenance operation of metallic structures [1]. The research presented in this paper is significant as it aims to enhance the performance of ECT systems. This improvement contributes to the safety and reliability of various engineering structures in aerospace, automotive, manufacturing, and infrastructure maintenance. The ECT system is a crucial tool for characterising metallic material properties, including surface and subsurface defects, thereby ensuring structural integrity and operational safety.

One of the significant challenges in ECT is the distance between the testing coil and the surface of the material under inspection, called the lift-off effect [1]. It occurs due to either surface roughness, vibrations, sensor misalignment, or other environmental disturbances. Its variation impacts the accuracy of defect detection and characterization by masking the defect features with noise. This reduces the signal-to-noise ratio (SNR) and sensitivity of the ECT system.

Several attempts have been made to separate the lift-off noise from the ECT signal, including the positioning of the sensor from the design approaches [2], unique lift-off invariant (LOI) features [3], and response and extracted features processing [4]. Additionally, a unique response feature, which is immune to lift-off variations such as LOI [3], the phase spectrum of the Pulsed ECT response [5], and novel compensation peak frequency feature [4] have been used for thickness measurement. However, each transmit (Tx) - receive (Rx) (Tx-Rx) ECT probe must conform to a particular structural arrangement for optimal lift-off inspection, depending on the Tx-Rx coil gap for a specific lift-off inspection [2] . Therefore, depending on the signal conditioning circuits, a given coil gap could optimally operate at a defined lift-off for a particular Tx-Rx coil arrangement in loose Tx and Rx coils,

The choice of signal conditioning circuit greatly influences the performance of the ECT system's Tx-Rx coil probe. Magnetic Resonance Circuit (MRC) is one of the signal conditioning circuits that enables maximum energy transfer between the Tx and Rx coils of the ECT system and the material under investigation. It uses multiple-resonance for multiple defect parameter information, even with the variation in lift-off distances. Therefore, this paper aims to assess various MRCs as signal conditioning circuits for ECT probes to enhance their performance at different lift-off distances. The focus is on comparing the lift-off performance of different MRC topologies of Wireless Power Transfer (WPT), including Series-Series (SS), Series-Parallel (SP), Parallel-Series (PS), Parallel-Parallel (PP), and Parallel/Series-Parallel/Series (PS-PS). This comparison aims to identify the optimal topology with multiple resonance capability and sensitivity to crack and sample influence for optimal response to crack parameters.

Previously, the WPT-based ECT using MRC topologies focused on defect detection and characterisation without much attention to the lift-off issues [6]. The first proof of concept investigated the capability of multiple resonances and

Manuscript received Month xx, 2xxx; revised Month xx, xxxx; accepted Month x, xxxx. This work was supported by the Petroleum Technology Development Fund (PTDF) Nigeria under scholarship award number PTDF/ED/PHD/DLU/1276/17

Lawal Umar Daura and Yichuang Sun are with the University of Hertfordshire, UK, AL10 9AB, U.K. (e-mail: l.u.daura@herts.ac.uk, y.sun@herts.ac.uk). Gui Yun Tian, Emmanuel T Ibrahim, and Changrong Yang are with the School of Engineering, Newcastle University, NE1 7RU, U.K. (e-mail: g.y.tian@newcastle.ac.uk, e.t.ibrahim2@newcastle.ac.uk, c.yang1@newcastle.ac.uk). Monika Roopak is with the University of Bedfordshire, UK (e-mail: monika.roopak@beds.ac.uk)).

characterization of crack parameters in Aluminium material. It used a series resonance WPT topology due to its low input and output impedance and ability to generate maximum current for the primary field [7]. Later, a parallel resonance WPT topology was employed to extract multiple features to characterize and map the 3D natural dent area caused by metal loss on a pipeline sample [8] due to its higher transfer response to metal and defect and less sensitivity to noise influence. Unlike [7] and [8], a combination of parallel and series resonance topologies was also applied to each of the Tx and Rx coils to characterize the rolling contact fatigue crack opening, propagation length, and inclined angle to the surface [9]. The series compensation was implemented to reduce the effective reactance of the Tx and Rx coils and share the total reactive power with shunt Tx and Rx compensation to maintain Tx and Rx current oscillation and improve impedance matching. The study extended the experimental setup of reference [9] by thoroughly comparing five MRC topologies for multiple resonance capability, analysing response sensitivity and robustness, and expanding feature extraction capabilities for enhanced measurement Signal-to-Noise Ratio (SNR) across varied non-destructive testing scenarios. Each MRC topology exhibits distinct frequency responses based on its reactive compensation arrangement, which in turn influences its performance and quality factors [10]. Therefore, it is important to understand the various MRC topologies when investigating unavoidable lift-off distance issues with ECT probe response evaluation. The probe performance based on extracted feature sensitivity will determine how well it can detect variations in defect parameters. At the same time, SNR will affect the clarity and reliability of the probe measurements.

This paper differs from the previous WPT-based ECT by addressing the critical challenge of lift-off in ECT by evaluating various MRC topologies to enhance defect detection accuracy. It introduces innovative signal conditioning circuits that improve the signal-to-noise ratio (SNR) and optimize response sensitivity across different lift-off distances. The comparative analysis of these topologies offers insights into their respective advantages and limitations, contributing to the optimized ECT systems. It provides both simulated theoretical and practical guidelines for developing more robust and reliable ECT systems in challenging lift-off conditions.

In the remaining sections of the article, section II details the integration of MRC topologies of WPT to ECT and its application to NDT. Section III presents the WPT-based ECT system's methods and experimental setup, including the system response. Section IV discusses the results of the system response and extracted features and demonstrates substantial improvements from the SNR of the extracted resonance point features. Finally, section V concludes with contributions to advance ECT defect detection and characterization for the safe operation of metallic structures.

II. MRC Topology of WPT Integration to ECT Probe

This section reviews the Tx-Rx coils of ECT inductive probes, which leads to different MRC topologies of WPT for Tx-Rx ECT probes, including their principles and motives. Finally, it investigates the simulated responses of different MRC topologies in the presence of metallic samples using the LTSpice circuit simulator.

A. Tx-Rx ECT Induction Probe

The ECT inductive probe comprises an excitation source($\boldsymbol{V_1}(v)$), Tx magnetic field ($\vec{\boldsymbol{B}}_{\boldsymbol{p}}(T)$), induced-eddy-current in the sample ($\vec{\boldsymbol{J}}_{\boldsymbol{eddy}}$), Rx magnetic field ($\vec{\boldsymbol{B}}_{\boldsymbol{eddy}}$), and induced-voltage ($\boldsymbol{V_2}$) to the Rx coil due to the influence of $\vec{\boldsymbol{B}}_{\boldsymbol{p}}(T)$ and $\vec{\boldsymbol{B}}_{\boldsymbol{eddy}}$. According to Maxwell's equations [11], (1) links the time-domain relationship between electrical variables and magnetic variables, as seen in Fig. 1. According to Fig. 1, the flow of current ($I_1(t)$) through Tx coil produces a field ($\overrightarrow{B_p}(r,t)$), which induces an eddy current with a density ($\vec{J}_{eddy}(r,t)$) on the surface of metallic material. Conversely, the produced magnetic field ($\vec{B}_{eddy}(r,t)$) from the induced eddy current links the Tx coil. According to Faraday's law, a voltage is said to induce in the Rx coil ($V_2\ (t)$) with a current ($I_2(t)$) due to the closed circuit. The field of eddy current density carries information related to the material properties, modulates $\vec{\boldsymbol{B}}_{\boldsymbol{p}}(T)$, and impacts the Tx and Rx impedances.

$$V_1(t) \rightarrow I_1(t) \rightarrow \overrightarrow{B_p}(r,t) \rightarrow \vec{J}_{eddy}(r,t) \rightarrow \vec{B}_{eddy}(r,t) \rightarrow I_2(t) \rightarrow V_2\ (t) \quad (1)$$

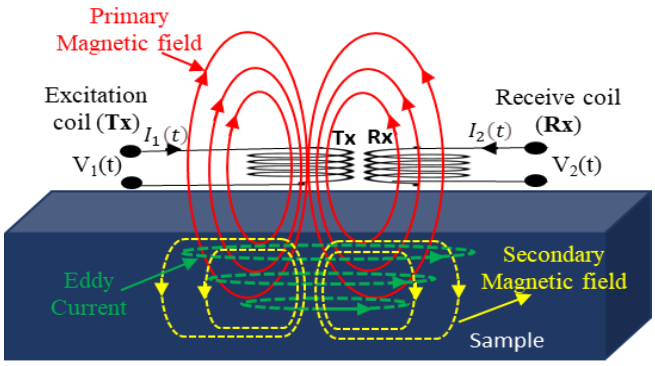

Fig. 1 Tx-Rx ECT probe and metallic materials, indicating excitation source (V1), induced eddy current and its generated (secondary) field, Tx generated (primary) fields, and induced Rx voltage (V2).

In a metallic conductor, the conduction current density (J = $\vec{\boldsymbol{J}}_{\boldsymbol{eddy}}$) surpasses the displacement current density by a substantial margin due to the absence of internal electric charge density (ρ) buildup within the conductor [12]. Therefore, the non-static Maxwell's equations are modified to yield a new expression that contains primary and secondary fields given in (2) [6].

Equation (2) conforms with the standard equation of non-homogeneous vector-Helmholtz in (3), which solves different excitations by specifying boundary conditions at infinity [12], where k^2 is constant and equals to $-\mathrm{j}\omega\mu\sigma$.

$$\nabla^2\vec{\mathrm{B}}_{\mathrm{eddy}} + (-\mathrm{j}\omega\mu\sigma)\vec{\mathrm{B}}_{\mathrm{eddy}} = \mathrm{j}\omega\mu\sigma\vec{\mathrm{B}}_{\mathrm{p}} \quad (2)$$

$$\nabla^2\vec{\mathrm{B}}_{\mathrm{eddy}} + \mathrm{k}^2\vec{\mathrm{B}}_{\mathrm{eddy}} = -\mathrm{k}^2\vec{\mathrm{B}}_{\mathrm{p}} \quad (3)$$

The eddy current generated field (B_{eddy}) carries information on the metallic material permeability, conductivity, and sample geometry, which changes the impedance of both the Tx and Rx coils. The changes in impedance affect the voltage and current in the transmitting (Tx) and receiving (Rx) coils. Therefore, it is necessary to use classical circuit theories to study the MRC

of the Tx-Rx network. This will help in analyzing material properties and other sensing applications. The paper discusses and presents the MRC of Tx-Rx coils in the following section.

B. MRC Topology for ECT applications

Magnetic Resonance Circuit (MRC) is a type of WPT topology that focuses on resonant Tx-Rx inductive coupling. It revolutionised Tx-Rx inductive WPT technologies due to the discovery by the Massachusetts Institute of Technology (MIT) in 2007 [13], which gave birth to various novel applications, including ECT sensing for NDT and evaluation of structural integrity [6-9]. Its application to ECT is based on the influence of the eddy current generated field from the sample on the power transfer between Tx and Rx coils according to the law of electromagnetic induction and Lenz's law. In this case, the ECT system operates at matching impedances, leading to maximum power transfer efficiency and the potential of splitting frequency response, depending on the Tx-Rx mutual coupling, among other factors [14].

Fig. 2 (a) to (d) shows the circuit connection diagrams of four basic MRC topologies, integrating the eddy current circuit from the metallic material described by the sample inductance (L_S) and resistance (R_S). C1 and C2 are the compensation capacitors connected to the Tx and Rx coils for controlling Tx and Rx resonance, respectively, while V is the excitation voltage. Likewise, RL and rs refer to the load and source impedances, respectively, while R1 and R2 represent the DC resistances of the Tx and Rx, respectively.

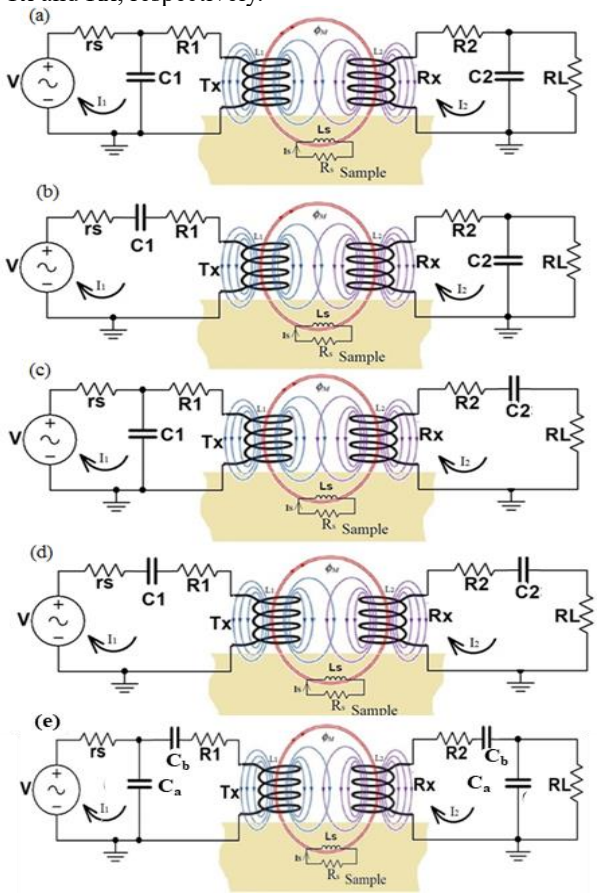

Fig. 2 Circuit diagram of the WPT-based ECT MRC topologies considered in this study (a) Parallel-Parallel (PP), (b) Parallel-Series (PS), (c) Series-Parallel (SP), (d) Series-Series (SS), and (e) PS-PS topologies

In the classical circuit theories applied to the MRC topologies shown in Fig. 2, three different current loops exist in each circuit. These are the Tx excitation current (I_1), Rx current (I_2), and the sample induced-eddy-current (Is) loops. Kirchhoff's laws described the loops in (4), which can be adjusted to include the dominant coil's parameters (self-inductances, L1/L2 and resistances, R1/R2) and sample inductance (L_S) and resistance (Rs) due to eddy-current disruption. The modified equation is described by the Tx voltage and Rx induced-voltage matrix and sample influences as seen in (5), where M_{12}, M_{1s}, and M_{2s} are the mutual inductances of the Tx-Rx coils, Tx-sample, and Rx-sample, respectively, while Z_1, Z_2, and Z_s are the self-impedances of the primary (Tx) circuit, seen from the primary source voltage, the secondary circuit (Rx), seen from the load RL side, and the metallic sample equivalent circuits, respectively. The self-impedances, Z_1 and Z_2, of each MRC topology differ and are fully described in ref. [15].

$$\begin{pmatrix} V \\ 0 \\ 0 \end{pmatrix} = \begin{pmatrix} Z_1 & -j\omega M_{12} & -j\omega M_{1s} \\ -j\omega M_{12} & Z_2 & j\omega M_{s2} \\ -j\omega M_{1s} & j\omega M_{s2} & Z_s \end{pmatrix} \begin{pmatrix} I_1 \\ I_2 \\ I_s \end{pmatrix} \quad (4)$$

$$\begin{bmatrix} V(\omega) \\ 0 \end{bmatrix} = \begin{bmatrix} Z_1 + \dfrac{(\omega M_{1s})^2}{Z_s} & Z_{12} \\ Z_{21} & Z_2 + \dfrac{(\omega M_{s2})^2}{Z_s} \end{bmatrix} \begin{bmatrix} I_1 \\ I_2 \end{bmatrix} \quad (5)$$

From (5), Z_{12} and Z_{21} are the forward and reverse transfer impedances that depend on the type of MRC. $Z_s(= R_s + j\omega L_s)$ is the metallic sample complex impedance due to material mechanical parameters, which testify R_s and $L_s$dependency on material conductivity and permeability, respectively. As in (5), the Tx and Rx behavior is modified by the influence of sample parameters, Zs (Rs and Ls) and mutual couplings, M_{1s} and M_{S2}. However, Zs depends on the defect parameters, sample geometry, and material type. Its effect is apparent in the voltage and current variables and their frequency responses. Therefore, sample nature and defect parameters influence the behaviour of eddy current density on the metallic sample due to their impact on the electromagnetic properties of the material, especially conductivity and permeability. The dynamic behavior of the WPT ECT system, as given by (5), is evaluated in our study using the scattering parameter, S_{21}, in the circuit simulation and experimental verification responses.

$$S_{21}(\omega, Lo) = 2\frac{V_L(\omega, Lo)}{V(\omega, Lo)}\sqrt{\frac{r_s}{RL}} \quad (6)$$

The S_{21} offers a better perception of measuring signal integrity at higher frequencies because of the skin depth challenge. In our study, we evaluate the performance of S_{21} considering the measuring instrument's constant source and load impedances and their dependency on frequency, sample characteristics and defect parameters. The potential of multiple peaks in the S_{21} response of the MRC of WPT-based ECT for a given frequency range depends on the input and output matching requirement, as well as the Tx-Rx parameters and coupling condition between Tx-Rx and the sample. The ratio of the output to input excitation voltages is proportional to the scattering parameter, S_{21}, given by (6) [8], which was evaluated in refs. [7] for SS, [8] for PP, and [9] for PS-PS topologies on different NDT&E applications. In (6), $V(\omega)$ and $V_L(\omega)$ are the excitation voltage

and output voltage across the load resistor (RL), respectively. The source, r_S and load, RL resistances are the characteristic impedances of port1 and port2 of the VNA, respectively, which are equal and constant.

Notably, the application of MRC to WPT-based ECT provides the unique attribute of having multiple feature points for multiple parameters, recognizing it as superior to other ECT systems. It facilitates efficient energy transfer between Tx and Rx coils, making it a standout choice in ECT applications.

In addition to the four basic topologies depicted in Fig. 2(a) to (d), this research includes a modified MRC topology, which combines series and parallel compensation for each Tx and Rx network, as shown in Fig. 2(e). The combined PS-PS topology was applied in ref. [9] to act as a resonance compensation and impedance matching at the same time. In comparing combined topology to single topology, one of the key advantages is that it helps to decrease the Tx coil's effective reactance by the series reactance, X_b. Additionally, it is beneficial in reducing the stress on parallel reactance, X_a, as it only contributes a portion of the total reactive power required to maintain the oscillation [16]. The modified topology is less sensitive to variations in the Tx-Rx parameter. Still, its remote eddy current field carries the conductivity, permeability, and geometric nature of the metallic sample in addition to the effect of lift-off distance. The PS-PS topology has a unique attribute; when $X_b < X_a$, more current passes through the Tx coil, and more voltage is induced in the Rx coil. Otherwise, a lower voltage is induced in the Rx coil.

Fig. 3 shows the simulated response of the five MRC topologies considered in this study. It demonstrates the capability of PP and PS-PS topologies of MRC for multiple resonances (dual peaks response) within the experimental parameters.

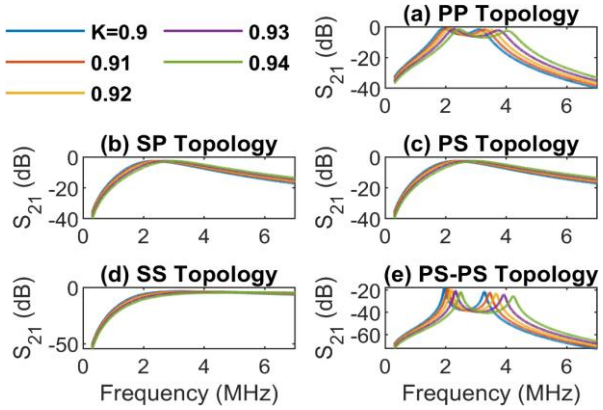

Fig. 3 LTSpice simulated S_{21} responses of the different MRC topologies at various coupling between Tx-Rx and sample for the WPT-based ECT MRC of Fig. 1 (a) to (e), respectively.

This paper simulates and experimentally compares five MRC WPT topologies to improve ECT responses for maximum energy transfer and multiple feature points. The simulated S_{21} responses evaluate coupling variations between Tx-Rx coils and the sample under different lift-off conditions. The experimental setup in the following sections mirrored the simulated parameters, verifying the topologies' LTSpice responses and comparing the S_{21} performance responses across topologies at different lift-off distances to mitigate lift-off sensitivity, which enhances feature selection based on SNR.

III. Experimental Setup and Methodology

In this section, five different MRC topologies for ECT probes are considered and designed to evaluate their potential for multiple feature points and lift-off performance for NDT&E of material properties and defects. The response of each probe was first simulated in the previous section for potentials of multiple-resonance and verified experimentally in this section.

A. MRC topology design and configuration

The first four MRC topologies presented in Fig. 2(a)-(d) have C1 and C2 compensating capacitors connected, either in series or parallel, to each of the Tx and Rx inductances (L1 and L2) to control the resonance point. The resonance frequency is analytically obtained by setting the imaginary part of the equivalent impedance of each Tx and Rx topology to zero. This frequency is given by (7) and (8) for series and parallel LC resonance, respectively. The parameters of the Tx and Rx coils are defined in Table I. The values of C1 and C2 were evaluated using an appropriately chosen 1 MHz resonance frequency due to the Tx/Rx natural resonance and frequency range of our measuring instrument, a network analyzer (E5071B). The probe's capability of responding to different lift-offs depends on the incident and reflected voltage measured by the S_{21} response. The values of the two compensating capacitors (C1 and C2) are evaluated to be 1.96 nf.

$$f_{0\_series} = \frac{1}{2\pi\sqrt{LiCi}} \tag{7}$$

$$f_{0\_parallel} = \frac{1}{2\pi}\sqrt{\frac{1}{LiCi} - \frac{Ri^2}{{L_i}^2}} \cong \frac{1}{2\pi}\sqrt{\frac{1}{LiCi}} \tag{8}$$

$$when\ \frac{1}{LiCi} \gg \frac{Ri^2}{Li^2}\ , i = 1\ for\ Tx\ and\ 2\ for\ Rx\ circuits$$

Similarly, for the PS-PS topology, Fig. 2(e) design, an input (*rs*) and output (*RL*) characteristic impedance of the VNA and the Tx - Rx coils' DC resistances (R1 and R2) are considered for evaluating the values of the two-compensating reactance, X_a and X_b for maximum power transfer conditions. The two compensating reactances determine the capacitors, C_a and C_b, respectively, based on (9) and (10) using the principle of the L-matching network [17]. Where the characteristic impedance of the VNA port is $Zc=R_c+jX_c=50+j0\ \Omega$ at port1 and port2. Q is the quality factor of the matching networks, which assigns a positive or negative (±) sign to show its dependency on required compensating conditions or configurations, as inductive or capacitive behaviour in the system. The evaluated parameters of the topologies and instruments of our experimental set-up are given in Table I.

$$X_a = -\frac{{R_c}^2 + {X_c}^2}{X_c + QR_c} = 1/(2\pi f C_a) \tag{9}$$

$$X_b = Qr_1 - X_1 = 1/(2\pi f C_b) \tag{10}$$

$$Where\ Q = \pm\sqrt{\frac{R_c}{r_1}\left(1 + \left(\frac{X_c}{R_c}\right)^2\right) - 1} \tag{11}$$

B. Experimental model

The experimental setup involves a wireless power transfer (WPT)-based eddy current testing (ECT) system utilizing an Agilent RF Network Analyzer (VNA-E5071B), Tx-Rx coils

configured in five different WPT topologies, and an XYZ scanner.

Fig. 4 illustrates the block diagram of the physical connection of the experimental devices, while Fig. 5 shows a picture of the experimental setup, including the fabricated metallic sample (Fig. 5(c)) and the coils of the Tx-Rx probe arrangement on the sample (Fig. 4(b)) for the investigation.

The system investigates crack detection in a fabricated sample by measuring the S_{21} response at varying lift-off distances between the transmitter (Tx) and receiver (Rx) coils. The coils are positioned coaxially with a fixed 0.2mm axial separation, ensuring higher mutual coupling than a side-by-side Tx and Rx coils configuration.

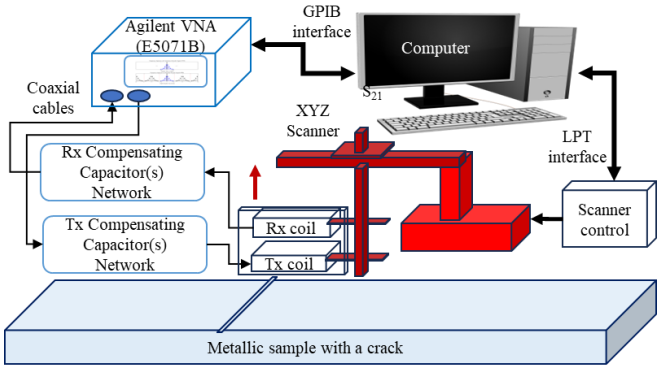

Fig. 4 Schematic diagram of experimental setup basic connection showing connection link between different devices

The Tx coil is connected to port1 of the VNA, and the Rx coil to port2, with the VNA providing the excitation signal. The setup tests five different compensating capacitor topologies: PP, PS, SP, SS, and PS-PS, using capacitors listed in Table I. The XYZ scanner moves the probe vertically from 0.0 mm to 11.8 mm 0.2 mm to gather data at 1601 frequency sample points.

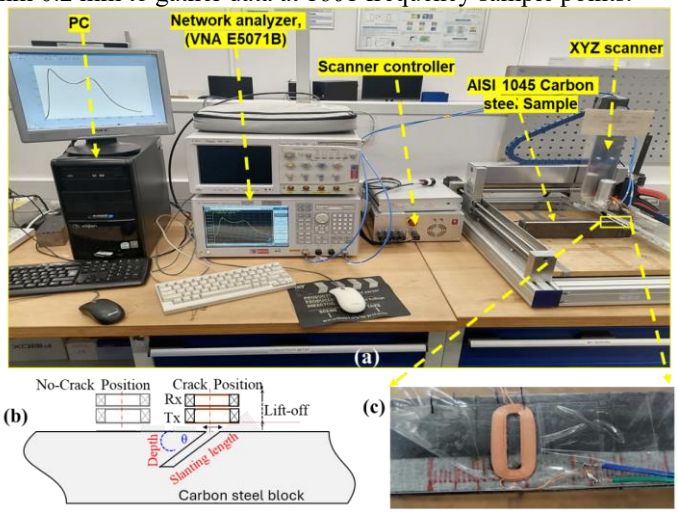

Fig. 5 Experimental setup diagrams consisting of (a) Photograph of the instruments and peripheral components (b) Arrangement of Tx-Rx, lift-off and sample with inclined crack parameters, L = slanting length, W = width, W0 = crack mouth/opening, d = depth, and θ = inclination angle (c) Carbon steel sample.

The VNA's consistent source and load impedances ensure that the sample's influence on the coupling to the Tx-Rx probe is accurately measured. Internally, the VNA converts signals into digital form through analog-to-digital converters (ADC) for each port, allowing high-resolution data capture. This data is processed, visualized on the VNA screen, and saved for further analysis on a computer.

The VNA's consistent source and load impedances ensure that the sample's influence on the coupling to the Tx-Rx probe is accurately measured. Internally, the VNA converts signals into digital form through analog-to-digital converters (ADC) for each port, allowing high-resolution data capture. This data is processed, visualized on the VNA screen, and saved for furtheranalysis on a computer.

TABLE I
TX-RX PROBE CONFIGURED PARAMETERS AND EXPERIMENTAL VARIABLES

Item	Value
PP, PS, SP, SS and PS-PS MRC topologies inductor (Manufacturer Part No.: IWAS3010AZEB130KF1)	Inductance: L1 = L2 = 12.90 µH
	Equivalent resistance: R1 = R2 = 0.70 Ω
	Dimension: 9.5 mm x 23.0 mm
PP, PS, SP, and SS MRCs	C1 = C2 = 1.96 nf
PS-PS MRC	C_a = 26.71 nf C_b = 1.96 nf
Design resonance frequency	f_0 (air) = 1 MHz
VNA Swept freq. excitation	0.5 MHz to 4.0 MHz, with 1601 frequency samples
Sample: AISI 1045 Carbon steel sample (300 mm × 30 mm × 63 mm)	
Measuring instrument: E5071B VNA, port1 and port2 with equal characteristic impedance ($X_c = 0$, $R_c = 50\ \Omega$)	
Investigated crack parameters: 450 inclined angle, 1.06 mm slanting height, 0.75 mm depth, and 0.43 mm opening width.	

The experimental results in Fig. 6 highlight the S_{21} responses at various lift-off points for the five different topologies, distinguishing between crack and no-crack conditions and indicating the extreme point as resonance feature positions. At each lift-off distance, the difference between the dashed response (representing no crack) and the non-dashed response (representing a crack) provides the crack signal without any lift-off noise. However, the frequency range of SS topology (Fig. 6(d)) extended beyond the range of the topologies' response to indicate a wider margin between crack and no-crack response with no potential for second resonance (peak) capability after the first resonance frequency point.

The PP and PS-PS topologies exhibit dual-peak responses due to their lower critical coupling points requirement for multiple resonances. In contrast, the PS, SP, and SS topologies primarily show single-peak responses. The SP topology's response is constrained by the secondary quality factor [14], while the SS topology exhibits a unique single peak due to its much lower

impedance requirement than that of the VNA port, in addition to minimal mutual coupling, as established by the simulated response in Fig. 3(d) and verified in Fig. 6(d).

The dual peak capability of PP and PS-PS is confirmed by the simulated and experimental responses. However, the slight difference between simulated and experimental resonant frequencies arises from parasitic effects and real-world tolerances, such as stray capacitances and variations in coil resistance, which are not present in simulations. The metallic sample's size also significantly influences S_{21} magnitude and resonance frequency, especially at varying lift-offs. The PS-PS topology's lower S_{21} magnitude reflects its design focus on impedance matching for signal robustness and noise suppression rather than maximizing the amplitude of the induced current response.

High eddy current density around the edges of the crack and the reduced value in the middle of the crack opening cause a larger S_{21} magnitude than the no-crack region across all the topologies due to the decreased electromagnetic coupling in the crack region. The experimental responses shown in Fig. 6 align with the simulated results presented in Fig.3 and are used to assess the sensitivity of each topology to crack detection. The simulated and experimental results confirmed that the PS-PS topology exhibits the lowest S_{21} response, reflecting its design prioritization of impedance matching and noise suppression, which ensures a superior Signal-to-Noise Ratio (SNR) and robust crack detection despite reduced raw amplitude.

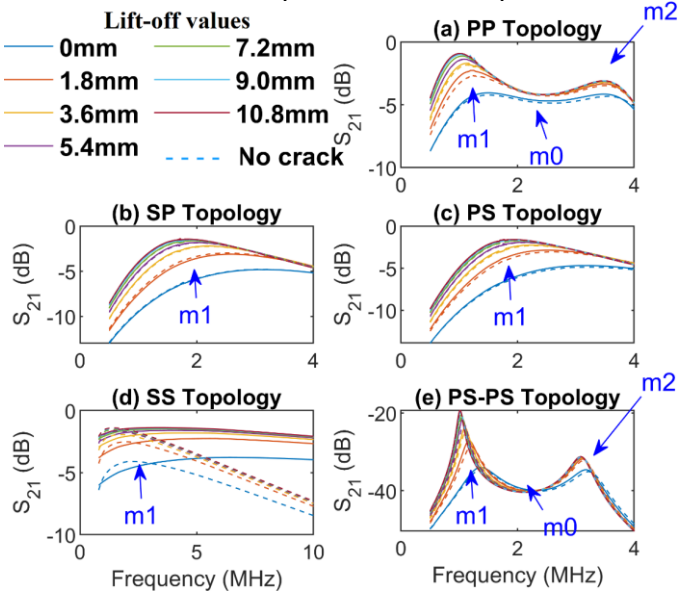

Fig. 6 Experimental S_{21} response of different MRC topologies at various lift-offs, indicating crack and no-crack for (a) PP, (b) SP, (c) PS, (d) SS, and (d) PS-PS topologies

IV. Results and Discussion

This section describes the responses of the five different MRC topologies, as shown in Fig. 6, to investigate sensitivity to response with a crack amidst various lift-offs, including resonance point feature extraction and extracted features' signal-to-noise ratio performance.

A. Response Sensitivity for Various Lift-off

The MRC responses of five WPT ECT topologies are further analysed for sensitivity to the crack and no crack positions at various lift-off distances in this section. The goal is to find the optimal topology that enables multiple resonance capability and sensitivity to crack and sample influence for optimal response to crack parameters.

By measuring the S_{21} parameter, the sensitivity of ECT system evaluation for probe lift-off to metallic material is possible due to the electromagnetic properties of the metal, such as permeability and conductivity, which limit the penetration due to skin depth. For thickness less than the skin depth, the entire thickness is involved in conducting the current. As the thickness increases beyond the skin depth, the additional thickness has less impact on the overall eddy current because it is confined to the surface layer, leading to the reflection of the magnetic flux by the test samples to induce more voltage on the sensor coil [2]. Similarly, increasing lift-off weakens the interaction between the magnetic field and the metallic sample. In our study, the reflected and incident voltages on the Tx-Rx coils, as defined by (6), due to the presence of a metallic sample, dictate the behaviour of the S_{21} response sensitivity at various lift-offs.

To evaluate the response sensitivity ($S_{21}S(L)$), as a change in the S_{21} parameter due to the presence of a crack, we compute the S_{21} parameter differences between the cracked and non-cracked positions for a range of sweeping frequency points and lift-off distances to get a relative change. Ultimately, we calculate the average relative change for all frequency points to get a single sensitivity value for each lift-off distance. Equation (12) [18] gives the average relative change in the S_{21} parameter due to the presence of a crack, normalised by the S_{21} parameter at the non-cracked position, for each lift-off distance.

$$S_{21}S(L) = \frac{1}{N}\sum_{i=1}^{N}\frac{S_{21C}(f_i, L) - S_{21NC}(f_i, L)}{S_{21NC}(f_i, L)} \qquad (12)$$

Where L is the lift-off distance, N is the number of frequency points (1601), $S_{21C}(f_i, L)$ is the S_{21} parameter at the cracked position for frequency (f_i) and lift-off distance (L) from 0.0 mm to 11.8 mm at an interval of 0.2mm, and $S_{21NC}(f_i, L)$ is the S_{21} parameter at the non-cracked position for frequency (f_i) and lift-off distance (L).

In Fig. 7, the S_{21} response sensitivity ($S_{21}S(L)$) of the five MRC topologies is described for various lift-offs from 0.0 mm to 11.8 mm at intervals of 0.2 mm. The graph shows that the PP, PS, SP, and PS-PS topologies' sensitivities to crack amidst various lift-offs are limited to lower than 4mm lift-off, with each topology achieving peak sensitivity around 0.6mm lift-off. As the lift-off increases, the sensitivity initially rises sharply. This sensitivity reaches its peak at an optimal lift-off point. The exact value of this optimal lift-off depends on factors such as the size of the coil and the gap between the transmitting (Tx) and receiving (Rx) coils [2]. Beyond this optimal point, further increasing the lift-off typically results in a decrease in sensitivity due to the weakening interaction between the electromagnetic field and the material. This behaviour is particularly demonstrated by the PS-PS topology, which has the lowest change in sensitivity for various lift-offs due to its design nature and the trade-off between lift-off robustness and defect detection sensitivity in the ECT system. The PP topology has

the highest sensitivity to cracks due to its high input and output impedance, strong electromagnetic coupling, and design focus on maximizing efficient induced-eddy-current signal amplitude, making it ideal for detecting small defects. However, the SS topology's sensitivity to the crack increases with higher lift-off distances due to its high current at resonance, resulting in strong magnetic fields linking the sample, making it susceptible to lift-off noise.

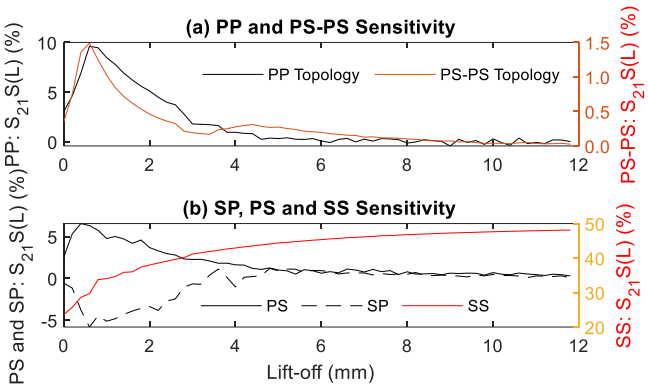

Fig. 7 S_{21} sensitivity to crack due to lift-off variation using different MRC topologies for (a) PP and PS-PS, (b) PS, SP, and SS topologies

B. Resonance Point Features (RPF)

The response of the MRC topologies provides either single or multiple peak magnitudes corresponding to resonance points, depending on the experimental condition and parameters. Fig. 6(a) – (e) indicates the three extrema points, m1, m0, and m2, corresponding to the first resonance magnitude for single and dual peak responses, the minima point magnitude for dual peak responses, and the second peak magnitude of the dual peak response, respectively. There is a corresponding frequency to every magnitude: f1 for the first peak, f0 for the minima point, and f2 for the second peak.

Using multiple resonance frequencies from the response of MRC topologies of WPT-based ECT systems can enhance defect detection accuracy by providing additional features at the optimal response for signal analysis. This approach allows for better characterization of defect dimensions and reduces the impact of noise.

Fig. 8 shows multiple features extracted from the S_{21} responses of the five MRC topologies at both crack and no crack positions, including m1, m0, m2, f1, f0, and f2 features for various lift-off positions. Generally, resonance point frequency features from the multiple resonance topologies (Fig. 8 (a) to (f)) are highly robust to lift-off compared to the single resonance topology (Fig. 8(g) to (i)). However, the response of the PS-PS topology is less sensitive to a crack (Fig. 7(a)).

In Fig. 8, the magnitude features (m1, m0, m2) are less affected by external noise than the frequency features (f1, f0, f2). This is due to the local variation of complex permeability around the crack edges, which complicates the ECT measurement by altering the eddy current field at a near lift-off distance. The resonance frequency features, f1, f0, and f2, from the responses of the five MRC topologies decrease as the lift-off increases from 0.0 mm to 11.8 mm. Conversely, the magnitude of the resonance points features, m1, m0, and m2, increases as the lift-off increases, except for m0 of the PS-PS MRC topology due to its combined series and shunt compensation reactance to each primary and secondary topology network. The first peak magnitude, m1, extracted from the response of the PS-PS MRC topology, exhibits the highest change in magnitude across lift-off distances from 0.0 mm to 11.8 mm, as shown in Fig. 8(d). This is attributed to the unique advantages of the PS-PS MRC topology, which efficiently supplies a portion of the total reactive power necessary to sustain the oscillation due to the combined advantages of the PP and SS MRC topologies [16].

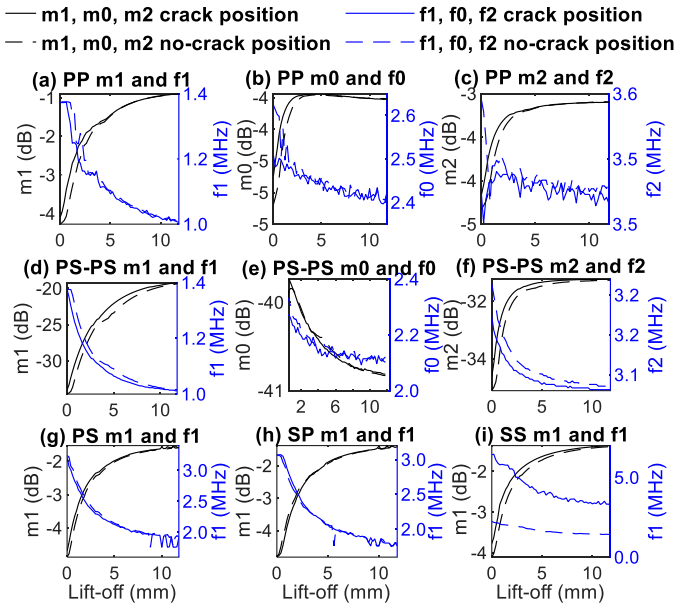

Fig. 8 Extracted resonance point features from the first peak magnitude, m1 and f1, minima point, m0 and f0, and second peak magnitude, m2 and f2 of (a) to (c) for PP topology, (d) to (f) for PS-PS, (g) for PS, (h) for SP, and (i) for SS topologies

C. Signal-to-Noise-Ratio (SNR)

This section evaluates the robustness of the MRC topology response for WPT-based ECT by measuring SNR performance to compare the level of a desired signal to that of background noise. The higher SNR value of the extracted features is vital for optimal system performance in characterizing material and crack parameters.

The SNR is affected by the changes in the transfer (impedance) function caused by variations in sample conductivity and noise due to changes in lift-off and other inherent offset signals of coils. The SNR for each extracted feature was defined and evaluated using equation (13) [9], where mi_C and mi_{NC} represent the extracted features for crack and non-crack positions, respectively, and i = 0, 1, or 2.

$$SNR = 20\,log_{10}\frac{|mi_C - mean(mi_{NC})|}{std(mi_{NC})} \qquad (13)$$

The comparison of SNR at various lift-offs for different MRC topologies of WPT-based ECT can quantitatively give an optimal lift-off with fewer noise features for material and defect characterization. Fig. 9 shows the SNR of the extracted resonance point features at different lift-off distances. Generally, resonance frequency features (f1, f0, and f2) are

more susceptible to lift-off variation than magnitude features due to their high sensitivity at resonance, which requires high-resolution measurement.

Compared to other topologies' features, the first peak features, m1 and f1, of the PS-PS, PS, SP and SS MRC topologies (Fig. 9(d), (g), (h), and (i) are highly immune to lift-off and other noise sources at the optimal lift-off point where the SNR is at a peak, except for f1 of the SS topology, which decays for increasing lift-off. The first resonance frequency feature, f1 of the PS-PS topology, provides the highest SNR of 49.9 dB, and is the most robust feature, exhibiting immunity to noise at a 3.4mm lift-off distance, as seen in Fig. 9(d).

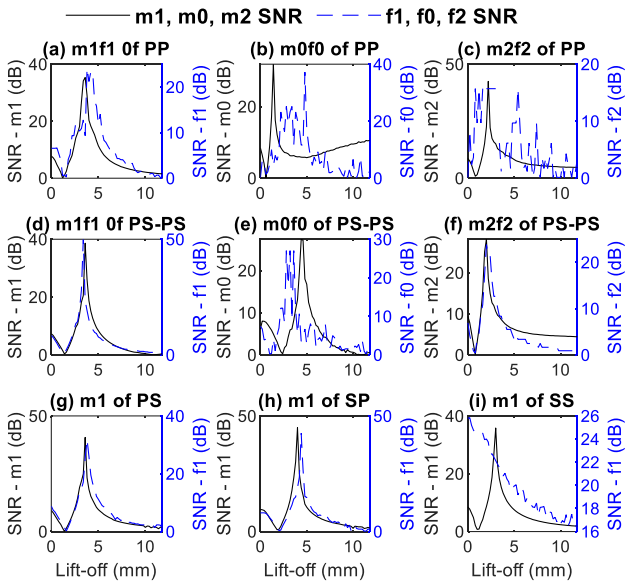

Fig. 9 SNR of the extracted resonance point features from the first peak magnitude, m1 and f1, minima point, m0 and f0, and second peak magnitude, m2 and f2 of (a) to (c) for PP topology, (d) to (f) for PS-PS, (g) for PS, (h) for SP, and (i) for SS topologies.

From the MRC topologies exhibiting dual peak responses, m0 has the smallest SNR value: 31.8 dB for PP and 27.2 dB for PS-PS topologies, compared to m1 and m2. Furthermore, the SNR of the f0 feature (Fig. 9(b) and (e)) exhibits variation across different lift-off positions, which could be due to a single reactive compensating element. However, that of the f2 in Fig. 9(c) could be due to the combined series and shunt reactive compensation.

Therefore, the optimal choice of Tx-Rx ECT probe depends on selecting the appropriate operating frequency and MRC topology, as well as robust features to mitigate lift-off and signal processing techniques that can minimize the adverse effects of lift-off while maximizing defect detection sensitivity. The PP topology is better at higher defect detection sensitivity and lift-off robustness, while the SS topology provides the highest sensitivity to defects at higher lift-offs due to the wide gap between crack and no-crack response signals for increasing lift-offs. The combined Topology (PS-PS) strikes a balance between lift-off robustness, leveraging multiple resonance frequency features to achieve an SNR of 49.9 dB with minimal change in lift-offs for most of its features.

D. SNR Performance Comparison

This work demonstrates superiority in various lift-off response sensitivity performances in ECT by achieving a maximum SNR of 49.9 dB at a 3.4 mm lift-off using one of the MRC topologies of WPT as a signal conditioning circuit. Compared to others, the proposed method achieved the highest using the minor crack depth to outperform other methods, although the higher the crack depth, the higher the SNR [19-22]. The other methods with the highest sensitivity, including the crack depth and lift-off, are presented in Table II. The maximum SNR of Pulsed Magnetic Flux Leakage [19] varied from 40.9 to 60.9 dB, depending on the position of the sensor, while that of other methods, like swept-frequency ECT [20], scanning induction thermography [21], and Near Electrical Resonance Signal Enhancement (NERSE) [22] had lower SNRs. This highlights the proposed method's superior performance in noise suppression for crack detection.

Table II
SNR COMPARISON TO THAT OF OTHER LITERATURE

Method	SNR (*dB*)	Crack depth (*mm*)	Lift-off (*mm*)
Proposed Method	49.90	0.75	3.40
NERSE ECT [22]	21.40	1.00	0.00
Pulsed Magnetic Flux Leakage. [19]	40.90 - 60.90	5.00	0.10
Swept-Frequency ECT [20]	22.80[a], 15.80[b]	3.00	3.00
Scanning Induction Thermography [21]	14.00	3.00	5.00

[a] *Time domain,* [b] *Frequency domain*

E. Lift-off Compensation Comparison

Table III summarises a comparison of other lift-off evaluations in terms of key innovations and applications with our proposed MRC topology for a WPT-based ECT system.

TABLE III
LIFT-OFF COMPENSATION KEY INNOVATION COMPARISON

Ref.	Method	Key Innovation	Application specific
[2]	Adaptive-frequency ECT	Conductivity invariance point control	Aerospace alloys
[3]	Pulsed ECT (PECT) time-domain analysis	Theoretical lift-off invariance proof	Foundation for PEC sensors
[4]	Pulsed ECT (PEC) signal compensation algorithm	Real-time lift-off error correction	Manufacturing quality assurance
[5]	Phase of the PECT spectral signal	Lift-off invariant	Pipeline thickness

		phase point (LIPP)	
[23]	Multi-frequency ECT	Lift-off invariant inductance (LII)	Steel defect detection
[24]	Dual-frequency ECT	Simultaneous lift-off & property measurement	Metal characterization
This work	Multiple resonance ECT	Multiple feature points and optimal lift-off	*Topology dependent

*MRC topologies application is critically influenced by material and defect characteristics, as demonstrated in our previous studies [7, 9], where angular railway cracks require a robust and modified topology that combines series and shunt (SP-SP) compensation for misalignment tolerance [9], while surface aluminium defects in [7] were efficiently detected using simpler SS resonance. Similarly, Environmental factors, such as lift-off caused by unavoidable vibration or surface unevenness, further dictate topology choices, with [25] and [8] showing SP-SP and PP topologies that excel in stable voltage delivery for high-resolution in flexible or noisy environments.

V. Conclusion

This study investigated the application of the resonance WPT concept integrated into an ECT probe for detecting cracks in metallic materials. It highlights the significance of optimal system performance amidst various lift-offs by integrating MRC topologies to enhance energy transfer efficiency, reduce inductive probe reactance stress, and improve system robustness in WPT-based ECT applications. Various MRC topologies, including PP, PS-PS, PS, SP, and SS, are evaluated for their response lift-off sensitivity to crack parameters and lift-off distances in ECT investigations, including extraction of multiple features and their immunity to lift-off using SNR performance metric. It offers an alternative approach for multiple parameter estimation, such as defects and lift-off measurements [26].

Based on the scope of this study, PP and PS-PS provide multiple resonance responses. However, PS-PS topology prioritizes impedance matching and noise suppression, achieving superior SNR and robust crack detection despite lower raw S_{21} amplitude, while the PP topology offers higher defect detection sensitivity at the cost of increased lift-off noise vulnerability.

The results are limited to the investigation of lift-off performance on surface and shallow subsurface defects using the Tx and Rx coils probe of ECT configured based on topologies of MRC of WPT. In the future, this research direction focuses on modifying MRC topologies for increasing sensitivity to crack parameters and improving SNR at higher lift-off variations, including various LOI points [2, 3] for improved ECT characterisation of cracks in engineering structures. Additionally, real-world noise factors and testing under varied environmental conditions are considered as future work, including frequency sweeping optimization by reducing the frequency range and increasing the sweeping speed using a planar eddy current probe to improve sensitivity and directivity for different crack orientations [27].

Reference

[1] A. N. AbdAlla, M. A. Faraj, F. Samsuri, D. Rifai, K. Ali, and Y. Al-Douri, "Challenges in improving the performance of eddy current testing: Review," *Measurement and Control,* vol. 52, no. 1-2, pp. 46-64, 2019, doi: 10.1177/0020294018801382.

[2] Z. Jin *et al.*, "Methods of Controlling Lift-Off in Conductivity Invariance Phenomenon for Eddy Current Testing," *IEEE Access,* vol. 8, pp. 122413-122421, 2020, doi: 10.1109/ACCESS.2020.3007216.

[3] G. Y. Tian, Y. Li, and C. Mandache, "Study of Lift-Off Invariance for Pulsed Eddy-Current Signals," *IEEE Transactions on Magnetics,* vol. 45, no. 1, pp. 184-191, 2009, doi: 10.1109/TMAG.2008.2006246.

[4] M. Lu, L. Yin, A. J. Peyton, and W. Yin, "A Novel Compensation Algorithm for Thickness Measurement Immune to Lift-Off Variations Using Eddy Current Method," *IEEE Transactions on Instrumentation and Measurement,* vol. 65, no. 12, pp. 2773-2779, 2016, doi: 10.1109/TIM.2016.2600918.

[5] M. Fan, B. Cao, A. I. Sunny, W. Li, G. Tian, and B. Ye, "Pulsed eddy current thickness measurement using phase features immune to liftoff effect," *NDT & E International,* vol. 86, pp. 123-131, 2017/03/01/ 2017, doi: https://doi.org/10.1016/j.ndteint.2016.12.003.

[6] L. U. Daura, "Investigation of Wireless Power Transfer-based Eddy Current Non-Destructive Testing and Evaluation," PhD Thesis, School of Engineering, Newcastle University, 2022. [Online]. Available: http://theses.ncl.ac.uk/jspui/handle/10443/5641

[7] L. U. Daura and G. Y. Tian, "Wireless Power Transfer Based Non-Destructive Evaluation of Cracks in Aluminum Material," *IEEE Sensors Journal,* vol. 19, no. 22, pp. 10529-10536, 2019, doi: 10.1109/JSEN.2019.2930738.

[8] L. U. Daura, G. Y. Tian, Q. Yi, and A. Sophian, "Wireless power transfer-based eddy current non-destructive testing using a flexible printed coil array," *Philosophical Transactions of the Royal Society A: Mathematical, Physical and Engineering Sciences,* vol. 378, no. 2182, p. 20190579, 2020, doi: doi:10.1098/rsta.2019.0579.

[9] L. U. Daura and G. Y. Tian, "Characterization of Angular RCF Cracks in a Railway Using Modified Topology of WPT-Based Eddy Current Testing," *IEEE Transactions on Industrial Informatics,* vol. 19, no. 4, pp. 5612-5622, 2023, doi: 10.1109/TII.2022.3201587.

[10] V. Shevchenko, O. Husev, R. Strzelecki, B. Pakhaliuk, N. Poliakov, and N. Strzelecka, "Compensation Topologies in IPT Systems: Standards, Requirements, Classification, Analysis, Comparison and Application," *IEEE Access,* vol. 7, pp. 120559-120580, 2019, doi: 10.1109/ACCESS.2019.2937891.

[11] M. Longair, "'...a paper ...I hold to be great guns': a commentary on Maxwell (1865) 'A dynamical theory of the electromagnetic field'," *Philosophical Transactions of the Royal Society A: Mathematical, Physical and Engineering Sciences,* vol. 373, no. 2039, p. 20140473, 2015, doi: doi:10.1098/rsta.2014.0473.

[12] J. R. Nagel, "Induced Eddy Currents in Simple Conductive Geometries: Mathematical Formalism Describes the Excitation of Electrical Eddy Currents in a Time-Varying Magnetic Field," *IEEE Antennas and Propagation Magazine,* vol. 60, no. 1, pp. 81-88, 2018, doi: 10.1109/MAP.2017.2774206.

[13] A. Kurs, A. Karalis, R. Moffatt, J. D. Joannopoulos, P. Fisher, and M. Soljačić, "Wireless Power Transfer via Strongly Coupled Magnetic Resonances," *Science,* vol. 317, no. 5834, p. 83, 2007, doi: 10.1126/science.1143254.

[14] Z. Zhang, H. Pang, A. Georgiadis, and C. Cecati, "Wireless Power Transfer—An Overview," *IEEE Transactions on Industrial Electronics,* vol. 66, no. 2, pp. 1044-1058, 2019, doi: 10.1109/TIE.2018.2835378.

[15] J. Sallan, J. L. Villa, A. Llombart, and J. F. Sanz, "Optimal Design of ICPT Systems Applied to Electric Vehicle Battery Charge," *IEEE Transactions on Industrial Electronics,* vol. 56, no. 6, pp. 2140-2149, 2009, doi: 10.1109/TIE.2009.2015359.

[16] S. Samanta and A. K. Rathore, "A comparison and performance evaluation of L-C and C-C-L compensation schemes on CSI based inductive WPT application," *2016 IEEE 25th International Symposium on Industrial*

Electronics (ISIE), pp. 817-822, 8-10 June 2016 2016, doi: 10.1109/ISIE.2016.7744995.

[17] M. Hirao and H. Ogi, "Brief Instruction to Build Emats," in *EMATs for Science and Industry: Noncontacting Ultrasonic Measurements*, M. Hirao and H. Ogi Eds. Boston, MA: Springer US, 2003, pp. 69-80.

[18] P. Li *et al.*, "Sensitivity boost of rosette eddy current array sensor for quantitative monitoring crack," *Sensors and Actuators A: Physical,* vol. 246, pp. 129-139, 2016/08/01/ 2016, doi: https://doi.org/10.1016/j.sna.2016.05.023.

[19] E. T. Ibrahim, C. Yang, G. Tian, M. Robinson, Q. Ma, and L. U. Daura, "Pulsed Magnetic Flux Leakage Measurement using Magnetic Head and Tunnelling Magnetoresistance for Defect Detection," *IEEE Sensors Journal,* pp. 1-1, 2023, doi: 10.1109/JSEN.2023.3297952.

[20] C. Ye, S. Laureti, H. Malekmohammadi, Y. Wang, and M. Ricci, "Swept-Frequency eddy current excitation for TMR array sensor and Pulse-Compression: Feasibility study and quantitative comparison of time and frequency domains processing," *Measurement,* vol. 187, p. 110249, 2022/01/01/ 2022, doi: https://doi.org/10.1016/j.measurement.2021.110249.

[21] H. Xia, J. Wu, Z. Xu, J. Wang, and C. Wang, "Defect Visualization and Depth Quantification in Scanning Induction Thermography," *IEEE Sensors Journal,* vol. 21, no. 9, pp. 10437-10444, 2021, doi: 10.1109/JSEN.2021.3060916.

[22] R. R. Hughes, Y. Fan, and S. Dixon, "Near electrical resonance signal enhancement (NERSE) in eddy-current crack detection," *NDT & E International,* vol. 66, pp. 82-89, 2014/09/01/ 2014, doi: https://doi.org/10.1016/j.ndteint.2014.04.009.

[23] M. Lu, X. Meng, R. Huang, L. Chen, A. Peyton, and W. Yin, "Lift-off invariant inductance of steels in multi-frequency eddy-current testing," *NDT & E International,* vol. 121, p. 102458, 2021/07/01/ 2021, doi: https://doi.org/10.1016/j.ndteint.2021.102458.

[24] M. Lu, X. Meng, R. Huang, L. Chen, A. Peyton, and W. Yin, "Measuring Lift-Off Distance and Electromagnetic Property of Metal Using Dual-Frequency Linearity Feature," *IEEE Transactions on Instrumentation and Measurement,* vol. 70, pp. 1-9, 2021, doi: 10.1109/TIM.2020.3029348.

[25] L. U. Daura, R. Monika, T. G. Yun, P. Simon, C. Xiaotian, and E. T. and Ibrahim, "Splitting frequency behavior of wireless power transfer for eddy current testing applications," *Nondestructive Testing and Evaluation,* pp. 1-21, 2025, doi: 10.1080/10589759.2025.2477682.

[26] G. Tian, C. Yang, X. Lu, Z. Wang, Z. Liang, and X. Li, "Inductance-to-digital converters (LDC) based integrative multi-parameter eddy current testing sensors for NDT&E," *NDT & E International,* vol. 138, p. 102888, 2023/09/01/ 2023, doi: https://doi.org/10.1016/j.ndteint.2023.102888.

[27] L. S. Rosado, T. G. Santos, P. M. Ramos, P. Vilaça, and M. Piedade, "A new dual driver planar eddy current probe with dynamically controlled induction pattern," *NDT & E International,* vol. 70, pp. 29-37, 2015/03/01/ 2015, doi: https://doi.org/10.1016/j.ndteint.2014.09.009.